

# Non-Markovian dynamics of the giant atom beyond the rotating-wave approximation

Mei Yu,<sup>1,\*</sup> Walter T. Strunz,<sup>1</sup> and Stefan Nimmrichter<sup>2</sup>

<sup>1</sup>*Institut für Theoretische Physik, Technische Universität Dresden, D-01062 Dresden, Germany*

<sup>2</sup>*Naturwissenschaftlich-Technische Fakultät, Universität Siegen, Siegen 57068, Germany*

Superconducting qubits coupled to meandering transmission lines or surface acoustic waves may realize giant artificial atoms, whose spatially separated coupling points give rise to long-lived non-Markovian dynamics. Previous studies were limited to the zero-temperature, weak-coupling regime, where the rotating-wave approximation applies and only single-phonon processes contribute. Here we go beyond these limits using the hierarchical equations of motion (HEOM). We show that HEOM accurately captures the exact dynamics at zero temperature and weak coupling, whereas perturbative Redfield theory fails due to long bath memory times. The non-Markovian effects persist at finite temperatures. In the strong-coupling regime, they are further enhanced, and we observe bound-state formation at zero temperature with only two coupling points. These results establish giant atoms as a powerful platform for exploring non-Markovian open quantum dynamics and their applications in quantum information and thermodynamics.

## I. INTRODUCTION

Recent advances in circuit quantum electrodynamics have enabled the realization of giant artificial atoms. These are superconducting qubits coupled to acoustic or photonic waveguides through several distinct contact points [1–5]. The spatially distributed coupling gives rise to several noteworthy phenomena beyond the conventional light-matter interaction. For instance, it leads to a sensitive frequency dependence of decay rates and Lamb shifts [6], the formation of bound states in the continuum [7–9], and non-reciprocal single-photon scattering [10]. Moreover, giant atoms can be engineered to support decoherence-free interactions [11, 12] and enable the generation of entanglement [13–16] between them. Beyond these effects, giant atoms provide a promising platform for open-system quantum simulation [17] and for realizing giant superatoms with protected entanglement manipulation and routing [18].

A key consequence of the extended spatial structure of giant atoms is the emergence of time-delayed feedback mechanisms [19, 20]. The finite propagation speed of phonons in an acoustic waveguide introduces a delay between the giant atom's emission of information at one contact point and its subsequent re-absorption at another one. This delay results in a memory effect that lets the atom's past state influence its future time evolution, a hallmark of non-Markovianity [21–23]. Experimental evidence of this behavior was obtained by observing the non-exponential relaxation of a giant atom [5]. The memory effect can be tailored by adjusting the distance between the coupling points, tuning the material properties of the waveguide, and manipulating the atom-waveguide coupling spectrum [3]. Moreover, the memory effect is phase coherent and thus genuinely non-classical [24], which could aid the development of quantum memory systems that preserve coherence over longer

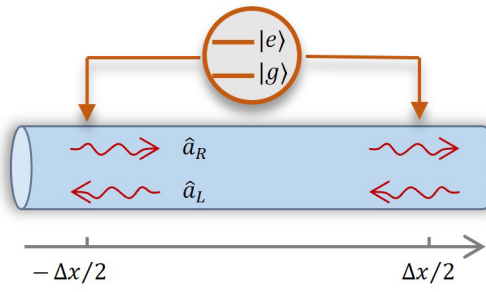


FIG. 1. Two-level giant atom coupled to the left- and right-propagating modes in a 1D acoustic waveguide via multiple contacts, with a separation of  $\Delta x$ .

timescales [25] and enable cycles of coherent energy exchange, for use in quantum thermal machines [26, 27] and entanglement harvesting [28–30].

Artificial giant atoms have gained significant interest due to their potential applications of non-Markovianity in quantum information processing [31, 32]. However, accurately describing their dynamics remains a major theoretical challenge, as strong memory effects from intricate feedback loops lead to the breakdown of conventional perturbative methods. At zero temperature, when the atom is weakly coupled to the acoustic field, the rotating-wave approximation (RWA) facilitates an analytical solution in the subspace of a single excitation in the field. The reduced atom dynamics can then be solved by integrating the full Schrödinger equation of "system+bath" [33]. The main difficulty is to go beyond the single-excitation assumption, involving multiple-phonon processes that arise, for example, in the strong coupling regime or at finite temperature. So far, to the best of our knowledge, this regime remains largely unexplored. Numerically exact approaches, such as matrix-product-state (MPS) simulations [19, 34], time evolving density operator with orthogonal polynomials algorithm (TEDOPA) [35], and the time-evolving matrix product operator (TEMPO) method [36, 37], or hierarchical approaches in terms of density operators (HEOM), or stochastic pure states

\* mei.yu@tu-dresden.de

(HOPS) [38] may offer potential routes toward tackling the fully non-perturbative dynamics.

In this work, we use the hierarchical equations of motion (HEOM) method [39–41] to exactly solve the dynamics of an artificial giant atom. The non-perturbative method works by expressing the bath correlation function (BCF) as a sum of exponential terms, giving rise to auxiliary density operators (ADOs). This results in a hierarchy of coupled differential equations that describe the system's evolution, which can be solved directly or using numerical tools like QuTiP [41]. In the considered setup, however, the bath correlation function exhibits a highly nontrivial structure that standard fitting methods, such as Matsubara spectral decomposition [42–44] and Padé spectral decomposition [45, 46], fail to capture accurately. To address this, we develop a fitting strategy tailored to the specific structure of our model, based on the estimation of signal parameters via rotational invariance technique (ESPRIT) [47, 48].

Using this fitting approach, we then simulate the giant atom dynamics and find excellent agreement between HEOM simulations and analytical results derived under the RWA and the single-excitation assumption in the weak-coupling, zero-temperature limit. In contrast, the Redfield master equation, a widely used perturbative method, fails to reproduce the correct dynamics in this regime, signaling the breakdown of perturbative treatments in the presence of strong non-Markovianity, i.e. long memory times. We further extend our analysis to finite temperatures within the weak-coupling regime and observe that the non-Markovian features of giant-atom dynamics persist even at elevated temperatures, demonstrating remarkable robustness against thermal fluctuations. Beyond the weak-coupling limit, we show that strong system–bath interactions further enhance memory effects and give rise to the formation of a bound state at zero temperature, a phenomenon characteristic to giant atoms.

The article is organized as follows: Section II introduces the physical model of a two-level giant atom coupled to a one-dimensional surface acoustic waveguide and discusses the challenges in obtaining an exact description of its reduced dynamics. Section III presents the HEOM approach used for numerical simulations. Section IV introduces the optimized ESPRIT fitting scheme and demonstrates its high accuracy for the considered spectral density. Section V benchmarks the HEOM results against analytical and perturbative solutions, while Sec. VI extends the method to finite temperatures and strong coupling. Conclusions are given in Sec. VII.

## II. GIANT ATOM MODEL

The model under consideration is based on the physical setup of Ref. [5] in which the non-Markovian excitation revivals of a giant atom were clearly observed for the first time. A superconducting transmon qubit with

resonance frequency  $\omega_0$  couples via two contact points of distance  $\Delta x$  to a transmission line of surface acoustic waves (SAWs) of velocity  $v_g$  on a piezoelectric substrate, as sketched in Fig. 1. The acoustic wavelength at the qubit resonance frequency is several orders of magnitude smaller than  $\Delta x$ . Introducing the characteristic time delay,  $\tau = \Delta x/v_g$ , we have  $\omega_0\tau \gg 1$ . The spectral coupling rate between the qubit and a running-wave SAW mode of frequency  $\omega$  modulates with the phase difference between the two contact points, ranging from a maximum  $\gamma(\omega)$  whenever  $\omega\tau = 0 \bmod 2\pi$  to zero when  $\omega\tau = \pi \bmod 2\pi$ . The corresponding Hamiltonian reads as [33],

$$\hat{H} = \hbar\omega_0|e\rangle\langle e| + \hbar \sum_{j=R,L} \int_0^\infty d\omega \omega \hat{a}_{j\omega}^\dagger \hat{a}_{j\omega} + \hbar \sum_{j=R,L} \int_0^\infty d\omega \sqrt{\frac{\gamma(\omega)}{\pi}} \cos\left(\frac{\omega\tau}{2}\right) \hat{\sigma}_x \left(\hat{a}_{j\omega}^\dagger + \hat{a}_{j\omega}\right). \quad (1)$$

Here, the operator  $\hat{\sigma}_x = \hat{\sigma}_- + \hat{\sigma}_+$  governs the interaction with the field, with  $\hat{\sigma}_- = |g\rangle\langle e|$  and  $\hat{\sigma}_+ = |e\rangle\langle g|$  the lowering and raising operators of the giant atom. The field operators  $\hat{a}_{j\omega}$  describe a continuum of right- ( $j = R$ ) and left-propagating ( $j = L$ ) SAW phonon modes, obeying the commutation relation  $[\hat{a}_{j\omega}, \hat{a}_{j'\omega'}^\dagger] = \delta_{jj'}\delta(\omega - \omega')$ . In the interaction picture, the Hamiltonian reduces to  $\hat{H}_I(t) = \hbar\hat{\sigma}_x(t)\hat{B}(t)$ , with  $\hat{\sigma}_x(t) = \hat{\sigma}_- e^{-i\omega_0 t} + h.c.$  and

$$\hat{B}(t) = \sum_{j=R,L} \int_0^\infty d\omega \sqrt{\frac{\gamma(\omega)}{\pi}} \cos\left(\frac{\omega\tau}{2}\right) \hat{a}_{j\omega}^\dagger e^{i\omega t} + h.c. \quad (2)$$

The memory effects of the field on the atom are fully characterized by the bath correlation function (BCF), given by

$$C(t) = \langle \hat{B}(t)\hat{B}(0) \rangle = \frac{1}{\pi} \int_{-\infty}^\infty d\omega J(\beta, \omega) e^{-i\omega t}, \quad (3)$$

$$J(\beta, \omega) = \frac{2\gamma(\omega)}{1 - e^{-\beta\omega}} \cos^2\left(\frac{\omega\tau}{2}\right), \text{ with } \gamma(\omega) = -\gamma(-\omega).$$

Here, the field is initially assumed to be in a thermal state with inverse temperature  $\beta = \hbar/k_B T$ . The effective bath spectral density function  $J(\beta, \omega)$  exhibits rapid oscillations on top of the slowly varying  $\gamma(\omega)$  due to interference between the two contact points. Hence, since the BCF is the Fourier transform of the effective spectral density, it features pronounced peaks at  $t = 0$  and  $t = \pm\tau$ . We shall adopt an Ohmic spectral density of the form  $\gamma(\omega) = \eta\omega e^{-\omega/\omega_c}$  with a dimensionless strength parameter  $\eta$  and a cutoff frequency that we set as  $\omega_c = 2\omega_0$ . This form reflects the linear dependence of the coupling strength on frequency as  $\omega \rightarrow 0$ , which naturally arises from the one-dimensional phonon density of states in surface acoustic waveguides. The exponential cutoff accounts for the finite bandwidth of the acoustic modes and regularizes the spectrum at high frequencies, ensuring both physical realism and mathematical convergence. The effective bath spectral density and the BCF

are plotted in Fig. 2 at zero temperature. As a result, in this setting, the field and the atom remain strongly correlated for an extended period, particularly when the time delay  $\tau$  is comparable to or longer than the atom's relaxation time. In the Markovian regime of zero delay and weak coupling,  $\tau = 0$  and  $\gamma(\omega_0) \ll \omega_0$ , the atom relaxes at a rate of  $\gamma(\omega_0)$ . Significant memory effects beyond the atomic lifetime are therefore expected to occur for  $\gamma(\omega_0)\tau \gtrsim 1$ , making it difficult in general to accurately describe the dynamics of the reduced atomic state.

### III. HEOM-BASED SIMULATED GIANT ATOM DYNAMICS

To simulate the dynamics of the giant atom, we employ the HEOM method, a non-perturbative approach designed to handle non-Markovian dynamics in open systems, particularly in the strong-coupling regime or when pronounced memory effects are present. The HEOM formalism relies on the assumption that the real and imaginary parts of the BCF can be approximated as a sum of exponentials,

$$C_R(t) \approx \sum_{k=1}^{N_R} c_k^R e^{-\gamma_k^R t}, \quad C_I(t) \approx \sum_{k=1}^{N_I} c_k^I e^{-\gamma_k^I t}, \quad (4)$$

where  $c_k^j$  and  $\gamma_k^j$  can be real or complex. Under this decomposition, the system's exact dynamics can be systematically derived using the influence functional approach [39–41]. Given an initial product state of system and phonon bath,  $\rho(0) = \rho_S(0) \otimes \rho_B(0)$ , one arrives at a hierarchy of coupled equations,

$$\begin{aligned} \frac{d}{dt} \rho_S^n(t) = & \left( -i\omega_0 |e\rangle\langle e|^{\times} - \sum_{j=R,I} \sum_{k=1}^{N_j} n_{jk} \gamma_k^j \right) \rho_S^n(t) \\ & - i \sum_{k=1}^{N_R} c_k^R n_{Rk} \hat{\sigma}_x^{\times} \rho_S^{n_{Rk}^-} + \sum_{k=1}^{N_I} c_k^I n_{Ik} \hat{\sigma}_x^{\circ} \rho_S^{n_{Ik}^-}(t) \\ & - i \sum_{j=R,I} \sum_{k=1}^{N_j} \hat{\sigma}_x^{\times} \rho_S^{n_{jk}^+}(t). \end{aligned} \quad (5)$$

Here, the superoperators  $O^{\times}$  and  $O^{\circ}$  are defined as  $O^{\times} \hat{A} = [\hat{O}, \hat{A}]$  and  $O^{\circ} \hat{A} = \{\hat{O}, \hat{A}\}$ , representing the commutator and anti-commutator actions, respectively. The multi-index  $n$  is given by  $n = (n_{R1}, n_{R2}, \dots, n_{RN_R}, n_{I1}, n_{I2}, \dots, n_{IN_I})$ , where each component  $n_{jk}$  is an integer within the range  $[0, N_c]$ , with  $N_c$  representing the truncation order for the numerical convergence. The density operator corresponding to  $n = (0, 0, \dots, 0)$  represents the reduced system state, while density operators with non-zero indices, referred to as auxiliary density operators (ADOs), encode the memory effect of the environment. The notation  $\rho_S^{n_{jk}^{\pm}}(t)$  indicates an ADO with a specific index either increased or decreased by one.

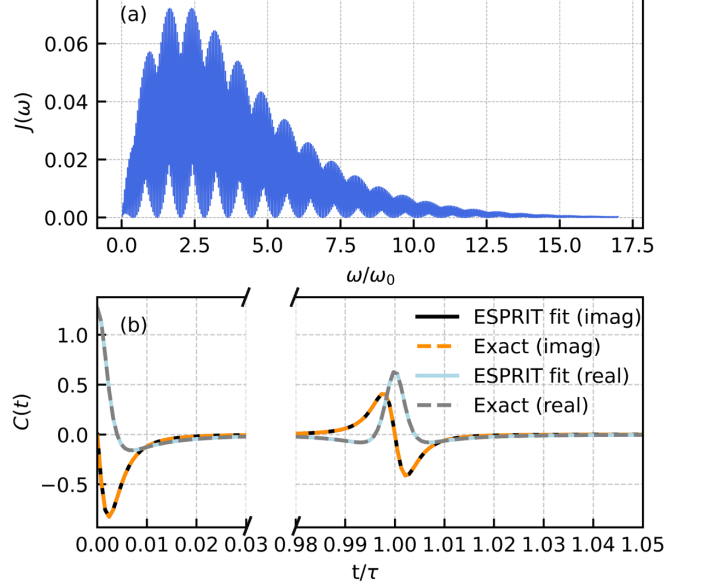


FIG. 2. (a) Effective bath spectral density of the SAW field at zero temperature; (b) The corresponding bath correlation function as function of time. Here and in the subsequent plots, we consider an Ohmic spectral density of the SAW environment,  $\gamma(\omega) = \eta \omega e^{-\omega/\omega_c}$ , with the coupling strength and cutoff frequency parameters set as  $\eta = 1 \times 10^{-2}$ ,  $\omega_c/\omega_0 = 2$  and  $\omega_0\tau/2\pi = 20$ .

Although the hierarchy formally contains an infinite number of equations, practical computations require truncation at a finite hierarchy depth  $N_c$ , beyond which higher-order terms have negligible contributions. The resulting finite set of coupled differential equations can be efficiently solved using standard numerical methods, as conveniently implemented in the HEOM module of the QuTiP framework [41]. Truncating the exponential decomposition of the BCFs (4) can introduce numerical artifacts, potentially leading to unphysical results and reducing the accuracy of the simulation. At the same time, to ensure computational efficiency, it is crucial to represent the BCF with as few exponential terms as possible while maintaining sufficient accuracy. Striking a balance between precision and computational cost is essential for the effective application of the HEOM method. Our simulations typically required several hundreds of exponential terms to converge, at a HEOM depth of  $N_c = 2$ .

### IV. EXPONENTIAL BCF DECOMPOSITION

Various numerical techniques have been developed to achieve an exponential decomposition of BCFs for use in HEOM, broadly categorized into frequency-domain and time-domain approaches. In the frequency domain, methods such as Matsubara frequency decomposition [42–44] and Padé spectral decomposition [45, 46] are commonly applied to simple spectral densities. However,

these methods often require numerous terms for convergence, particularly at low temperatures, where the Fano spectrum decomposition [49, 50] and Free-pole decomposition [51] are often more effective. Time-domain methods, including least squares fitting [52–54], and Prony’s method [55, 56], excel in localized fitting and are well suited for short-to-medium time behavior. However, they may encounter difficulties when applied to highly structured or multi-peaked BCFs.

Given the Ohmic spectral density  $\gamma(\omega)$  we consider for both contact points, the BCF (3) takes the analytical form,

$$C(t) = \frac{\eta}{2\pi\beta^2} \left\{ 2\Psi\left[1, \frac{1+i\tau\omega_c}{\beta\omega_c}\right] + 2\Psi\left[1, \frac{r}{\beta\omega_c}\right] \right. \\ + \Psi\left[1, \frac{1+i(t-\tau)\omega_c}{\beta\omega_c}\right] + \Psi\left[1, \frac{1+i(t+\tau)\omega_c}{\beta\omega_c}\right] \\ \left. + \Psi\left[1, \frac{r+i\tau\omega_c}{\beta\omega_c}\right] + \Psi\left[1, \frac{r-i\tau\omega_c}{\beta\omega_c}\right] \right\}. \quad (6)$$

with  $r = 1 - i\tau\omega_c + \beta\omega_c$ . Here,  $\Psi[1, x]$  denotes the first derivative of the digamma function [57]. As illustrated in Fig. 2(b), the BCF (6) exhibits sharp peaks at distinct times (integer multiples of the delay time  $\tau$ ), with a flat region between them. This structure poses significant challenges for the aforementioned decomposition methods, particularly as larger time delays accentuate the distinctness of the peaks, making an accurate representation more difficult.

In this work, we develop an optimized fitting scheme based on the ESPRIT algorithm [47, 48]. The method is refined to efficiently represent both the real and imaginary parts of the BCF (6) with a sum of exponential functions as in Eq. (4). The ESPRIT algorithm exploits the rotational invariance property of a Vandermonde matrix constructed from time-domain samples of the BCF. The procedure begins with sampling the BCF on a discrete-time grid, followed by the formation of a Hankel matrix from these samples. Singular value decomposition (SVD) is then applied to estimate the number of exponential components. In general, a direct ESPRIT fit tends to yield a redundant set of exponentials. To address this, we iteratively refine the fitted components by gradually reducing the number of terms while monitoring the relative fitting error. The iteration terminates once a closeness condition based on the  $L^2$ -norm is satisfied,  $\|C_{\text{fit}}(t) - C(t)\|_2 / \|C(t)\|_2 < \varepsilon_r$ , ensuring an accurate and compact exponential representation of the BCF. Reducing the threshold  $\varepsilon_r$  improves the accuracy of the fit, but requires a greater number of exponential functions to achieve this precision. Subsequently, the decay rates  $\gamma_k^R$  and  $\gamma_k^I$  are determined by solving an eigenvalue problem, while the corresponding amplitudes  $c_k^R$  and  $c_k^I$  are obtained via a least-squares fitting approach. By reconstructing the BCF as a sum of exponential functions, the optimized ESPRIT algorithm proves to be a robust and effective tool for time-domain analysis. This is demon-

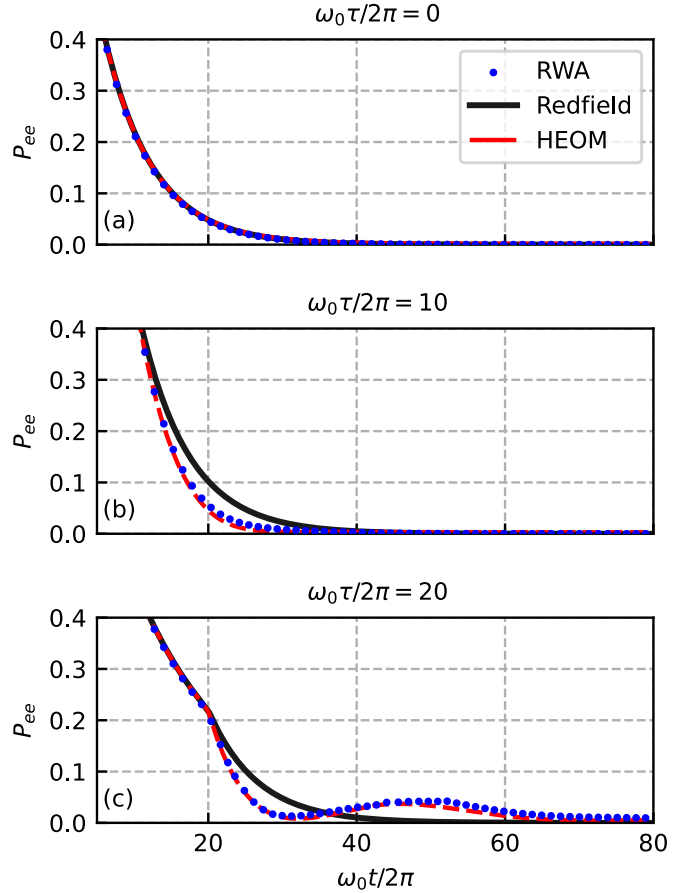


FIG. 3. Excited-state probability of the giant atom as a function of time, obtained from the RWA analytical solution, the Redfield master equation, and from HEOM simulations at zero temperature. We compare three different time delays  $\tau$ : (a) zero time delay, which amounts to a single contact point; (b) time delay comparable to the atomic relaxation time; (c) time delay longer than the atomic relaxation time. The other parameters are chosen as in Fig. 2.

strated in Fig. 2(b), where the real and imaginary components of the original and optimized ESPRIT-fitted BCF show excellent agreement. The plot emphasizes the non-zero regions, focusing on the short-time decay and the oscillatory behavior near  $t/\tau \approx 1$ , excluding the intermediate flat region for visual clarity. For this fitting, we set the relative error threshold at  $\varepsilon_r = 10^{-3}$ , balancing accuracy and computational efficiency.

While the optimized ESPRIT method effectively fits the BCF using a sum of exponentials, it often introduces a large number of terms, especially for a long time delay parameter  $\tau$ . This leads to a high-dimensional hierarchy in HEOM simulations, significantly increasing computational demands and making numerical integration more expensive. Thus, further optimizing the ESPRIT method to minimize the number of terms while preserving accuracy could be an important avenue for future research. Reducing the number of exponential components would enhance the computational efficiency of HEOM

simulations, making numerical integration less demanding and more practical for larger systems or extended time frames.

Using the fitting results, we then simulate the dynamics of a two-level giant atom with the HEOM implementation in QuTiP. To validate our numerical approach, we first perform a benchmark at zero temperature, where an analytical solution is available in the RWA regime.

## V. BENCHMARK AT ZERO TEMPERATURE

We shall investigate the dynamics of a two-level giant atom at zero temperature using different methods, focusing on the weak coupling regime. In the absence of thermal excitations, spontaneous emission arises due to the atom's interaction with vacuum fluctuations of the acoustic field. Under these conditions, the rotating wave approximation is justified and the analysis can be confined to the single-excitation subspace of the field. See App. A for a derivation of the exact time evolution in this setting. Equivalently, the time evolution of the giant atom state can be expressed in terms of a time-local non-Markovian master equation,

$$\frac{d\rho_S}{dt} = -i(\omega_0 + h(t))[\hat{\sigma}_+ \hat{\sigma}_-, \rho_S] + \gamma_-(t)\mathcal{D}[\hat{\sigma}_-]\rho_S \quad (7)$$

where  $h(t) = -\text{Im}[\dot{G}(t)/G(t)]$  is the Lamb shift, which renormalizes the system energy, and  $\mathcal{D}[\hat{\sigma}_-]\rho_S(t) = 2\hat{\sigma}_-\rho_S(t)\hat{\sigma}_+ - \{\hat{\sigma}_+ \hat{\sigma}_-, \rho_S(t)\}$  is the dissipator describing the spontaneous emission of the giant atom with a time-dependent decay rate  $\gamma_-(t) = -\text{Re}[\dot{G}(t)/G(t)]$ . The Green function  $G(t)$  satisfies the equation

$$\dot{G}(t) = -\int_0^t ds C(s)G(t-s)e^{i\omega_0 s}, \quad (8)$$

with initial condition  $G(0) = 1$ . This time-local master equation is exact in the sense that its generator contains the full Dyson series in the coupling strength, including all higher-order terms. This is crucial in regimes where the bath correlation time is sufficiently large that higher-order contributions cannot be neglected [58]. The non-Markovianity of the master equation is signified by transient negativities of  $\gamma_-(t)$  that may occur for  $\tau > 0$  [23, 59].

In the weak-coupling regime, one often employs the Redfield master equation as a perturbative approximation of the atom dynamics, retaining only the second-order term in the Dyson expansion of the generator. It has the same form as Eq. (7), but with the Lamb shift and decay rate given by their perturbative expressions

$$h(t) = \text{Im}[\Gamma_-(t)], \quad \gamma_-(t) = \text{Re}[\Gamma_-(t)],$$

$$\text{with } \Gamma_-(t) = \int_0^t ds C(s)e^{i\omega_0 s}; \quad (9)$$

see App. B for details. The Redfield master equation is more general than the Lindblad master equation, as

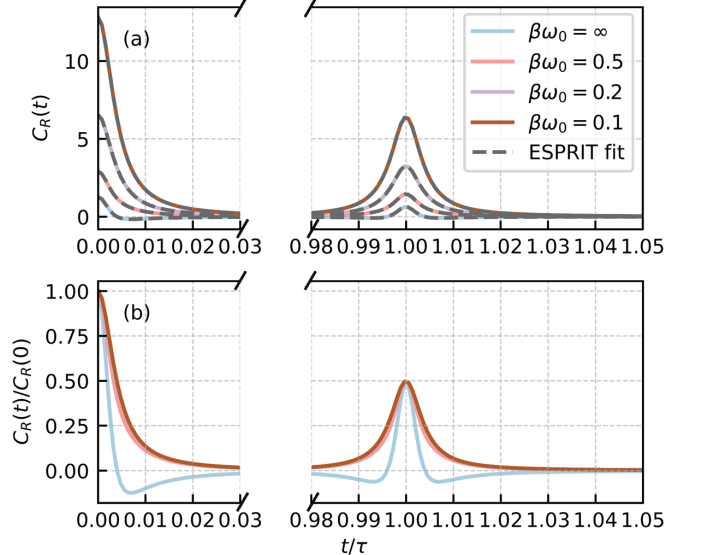


FIG. 4. (a) Real part of the thermal BCF for the SAW field as a function of time at various temperatures, along with their corresponding ESPRIT fits (dashed). (b) Rescaled thermal BCFs. All other parameters are the same as in Fig. 2.

it can account for bath memory effects that the Lindblad formalism inherently neglects. It has been shown to provide the most accurate description of the two-spin-boson model and the heat transport between two thermal baths mediated by two coupled oscillators in the weak-coupling regime [60, 61]. However, as we demonstrate below, the Redfield approach may still fail even at weak coupling strengths, when the propagation delay  $\tau$  becomes comparable to or exceeds the atomic relaxation time. The latter is defined as the inverse spontaneous emission rate in the Markovian limit at zero temperature,  $\gamma_-^{-1} = [2\gamma(\omega_0) \cos^2(\omega_0\tau/2)]^{-1}$ .

Figure 3 shows the time evolution of the excitation probability of a two-level giant atom,  $P_{ee} = \langle e | \rho_S | e \rangle$ , at zero temperature and for three chosen time delay parameters  $\tau$ . The atom is initially prepared in the excited state. We compare the exact solution under the RWA (blue dotted), the Redfield master equation (black solid), and the HEOM simulation (red dashed). Concerning the QuTiP HEOM implementation, the real and imaginary parts of the BCF at zero temperature are expanded into exponential terms using the ESPRIT method, as illustrated in Fig. 2(b). To ensure convergence of the HEOM simulation, we increased the number of ESPRIT fit terms from  $(N_R, N_I) = (6, 7)$  in (a) to  $(375, 378)$  in (b) and  $(743, 750)$  in (c), while keeping the simulation depth fixed at  $N_c = 2$ .

In the Markovian case of zero delay time in Fig. 3(a), the excitation probability exhibits simple exponential decay, with all three methods showing excellent agreement. In contrast, the non-Markovian regime, in which the delay time (b) is comparable to or (c) exceeds the atomic relaxation time, leads to clear deviations from exponential

decay. The Redfield master equation is then no longer accurate, and in particular, it fails to capture any excitation revivals in case (c), underscoring its limitations in modeling long-time memory effects. The numerically exact simulations on the other hand agree well with the RWA single-photon analytical results. HEOM is therefore well-suited for extensions to finite temperatures and stronger couplings, where an analytical solution based on the single-phonon assumption is no longer available.

## VI. MULTI-PHONON REGIME

We now consider the giant atom in a regime in which multi-phonon processes become significant, either due to the presence of thermal excitations of the SAW field or due to the ability of atomic transitions to excite multiple phonons. Such conditions could be achieved experimentally at higher temperatures and interactions strengths [62].

We begin by simulating the effect of a finite temperature on the giant atom dynamics at weak coupling using HEOM and examine how thermal fluctuations influence the population of ground and excited state and the coherence between them. The temperature enters via the Ohmic BCF (6), which we fit with an adequate number of exponential functions, as we did at zero temperature.

The thermal behaviour and the quality of the fit are illustrated in Fig. 4(a), which depicts the real part of the BCF  $C_R(t)$  as a function of time for various inverse temperatures  $\beta\omega_0$ , including the zero-temperature case  $\beta \rightarrow \infty$ . In contrast, the imaginary part of the correlation function is temperature-independent and coincides with its zero-temperature form. First, we notice that the overall amplitude of the BCF grows with temperature, scaling roughly in proportion to  $1/\beta\omega_0$  when  $\beta\omega_0 \ll 1$ . To highlight the temperature dependence of the  $C_R(t)$  shape, Fig. 4(b) presents the normalized curves  $C_R(t)/C_R(0)$ . The shape of the BCF also changes: the peaks around  $t = 0$  and  $\tau$  broaden with growing temperature and, unlike at zero temperature [see Fig. 2(b)], the peak tails are no longer negative for  $\beta\omega_0 < 2$ . The peak ratio stays at  $C_R(0)/C_R(\tau) \approx 2$  as long as the memory time is large,  $\omega_0\tau \gg 1$ . The dashed lines in Fig. 4(a) show the ESPRIT fits, which replicate  $C_R(t)$  accurately across all temperatures. As the structure of the BCF simplifies with growing temperature, the number of exponential fit terms can be reduced. The four plotted fits were obtained with  $(N_R, N_I) = (743, 750), (645, 750), (573, 750)$ , and  $(545, 750)$  in order of decreasing  $\beta$ .

With the BCF fits at hand, we can simulate the evolution of the two-level giant atom using HEOM. Fig. 5(a) and (c) show the time evolution of the excited state population,  $P_{ee}(t) = \langle e|\rho_S(t)|e \rangle$ , and the coherence,  $P_{eg}(t) = \langle e|\rho_S(t)|g \rangle$ , respectively, for a fairly weak coupling strength  $\eta = 10^{-2}$ . The atom is initialized in the superposition state  $|+\rangle = (|g\rangle + |e\rangle)/\sqrt{2}$ . In (a), the dashed lines mark the Gibbs steady-state population for

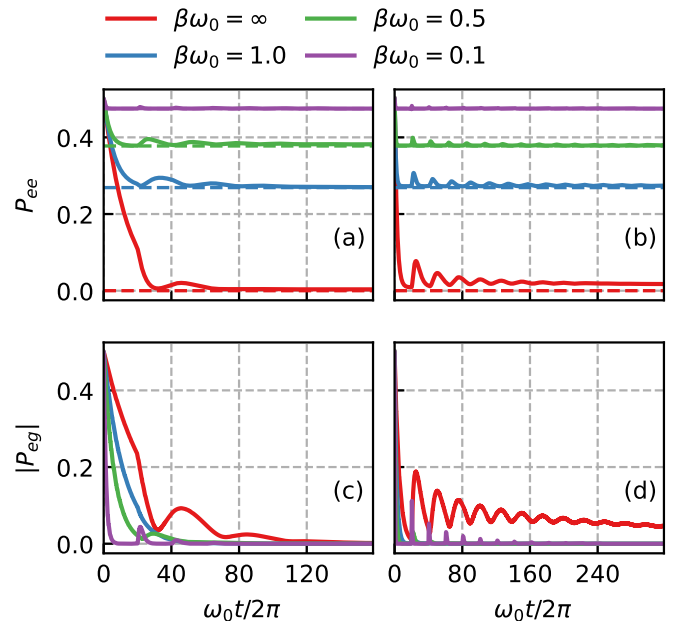


FIG. 5. Time evolution of the excited-state population  $P_{ee}$  [panels (a), (b)] and coherence  $|P_{eg}|$  [panels (c), (d)] of a two-level giant atom at different temperatures. Results are shown for weak coupling ( $\eta = 1 \times 10^{-2}$ , left column) and stronger coupling ( $\eta = 5 \times 10^{-2}$ , right column). All other parameters are the same as in Fig. 2.

each temperature, which is reached at long times. In (c), the coherence decays more rapidly with growing temperature. Nevertheless, revivals in both population and coherence persist, albeit with reduced amplitude and faster damping. This resilience of the memory effect against thermal noise constitutes a key feature of giant atom systems, which lends itself to benchmarking numerical or approximate techniques for non-Markovian open systems.

We now turn to the role of stronger coupling. The atom-bath coupling strength  $\eta$  enters the BCF (6) merely as a prefactor. Greater  $\eta$ -values thus result in a higher number of more pronounced revivals in both excitation and coherence, but with a faster decay of each such revival. This is illustrated in Fig. 5(b) and (d), which display the evolution of both quantities for a five times stronger coupling than in (a) and (c). Remarkably, in the low-temperature regime, we not only observe the clearest non-Markovian features, but also the onset of systematic deviations from the equilibration to a diagonal Gibbs state with respect to the bare atom Hamiltonian. Indeed, the strong-coupling regime can result in corrections described by the Hamiltonian of mean force [63, 64]. In our case of moderately strong coupling, this behavior can be confirmed by explicitly computing the mean-force Hamiltonian using a perturbative expansion; see App. C. At zero temperature, we even find a residual amount of coherence that persists over long times, which we attribute to the partial localization of the emitted

phonons around the atom due to interference between the two coupling points. At sufficiently strong coupling, these phonons can sustain a repeated coherent interaction with the atom, thereby forming a long-lived bound state between the atom and the SAW continuum with a finite amount of excitation and coherence in the atom. It was shown before that such bound states can even form in the weak-coupling limit when there are three or more coupling points to the waveguide [65]. Here we find that at stronger coupling, a long-lived state may appear even for two contact points only.

## VII. CONCLUSION

In conclusion, we have investigated the non-Markovian dynamics of an artificial giant atom coupled to one-dimensional surface acoustic waves using the HEOM method, which enables exact simulations beyond the rotating-wave and weak-coupling approximation. To validate our approach, we first benchmarked the HEOM results against analytical solutions in the zero-temperature, rotating-wave limit, finding excellent agreement and thereby confirming the accuracy of the method. In contrast, the perturbative Redfield master equation exhibits noticeable deviations from the exact dynamics, revealing its limitations even within the weak-coupling regime, due to long memory times.

By employing the HEOM framework, we extended our analysis to finite temperatures and stronger coupling

regimes. The results show that non-Markovian features remain remarkably robust against thermal noise and become further enhanced as the system–bath coupling increases. Moreover, in the strong-coupling regime, we identified the formation of atom–field bound states at zero temperature for only two contact points, a distinctive feature of giant-atom physics responsible for population trapping and long-lived coherence.

Our findings demonstrate that HEOM provides a powerful and reliable tool for exploring giant-atom dynamics in regimes inaccessible to perturbative treatments. This approach opens a pathway for quantitatively studying memory effects, and environment engineering in emerging quantum acoustic and waveguide QED platforms [5, 19, 20]. Future extensions may include studies of collective emission in multi-giant-atom networks coupled to a common reservoir, interactions with various structured environments, and driven nonequilibrium dynamics [66, 67]. It would also be interesting to investigate how quantum memory effects in giant-atom dynamics remain at finite temperatures, following the frameworks proposed in Refs. [24, 68]. Such directions would further advance the development of controllable non-Markovian platforms for quantum information processing and quantum thermodynamics.

## ACKNOWLEDGMENTS

M.Y. would like to thank Valentin Link and Hai-Chau Nguyen for helpful discussions. The University of Siegen is kindly acknowledged for enabling our computation through the OMNI cluster.

---

[1] L. Du, Y. Zhang, J.-H. Wu, A. F. Kockum, and Y. Li, Giant atoms in a synthetic frequency dimension, *Phys. Rev. Lett.* **128**, 223602 (2022).

[2] A. M. Vadiraj, A. Ask, T. G. McConkey, I. Nsanzineza, C. W. S. Chang, A. F. Kockum, and C. M. Wilson, Engineering the level structure of a giant artificial atom in waveguide quantum electrodynamics, *Phys. Rev. A* **103**, 023710 (2021).

[3] B. Kannan, M. J. Ruckriegel, D. L. Campbell, A. Frisk Kockum, J. Braumüller, D. K. Kim, M. Kjaergaard, P. Krantz, A. Melville, B. M. Niedzielski, *et al.*, Waveguide quantum electrodynamics with superconducting artificial giant atoms, *Nature* **583**, 775 (2020).

[4] R. Manenti, A. F. Kockum, A. Patterson, T. Behrle, J. Rahamim, G. Tancredi, F. Nori, and P. J. Leek, Circuit quantum acoustodynamics with surface acoustic waves, *Nature communications* **8**, 975 (2017).

[5] G. Andersson, B. Suri, L. Guo, T. Aref, and P. Delsing, Non-exponential decay of a giant artificial atom, *Nature Physics* **15**, 1123 (2019).

[6] A. Frisk Kockum, P. Delsing, and G. Johansson, Designing frequency-dependent relaxation rates and lamb shifts for a giant artificial atom, *Phys. Rev. A* **90**, 013837 (2014).

[7] S. Guo, Y. Wang, T. Purdy, and J. Taylor, Beyond spontaneous emission: Giant atom bounded in the continuum, *Phys. Rev. A* **102**, 033706 (2020).

[8] L. Guo, A. F. Kockum, F. Marquardt, and G. Johansson, Oscillating bound states for a giant atom, *Phys. Rev. Res.* **2**, 043014 (2020).

[9] W. Zhao and Z. Wang, Single-photon scattering and bound states in an atom-waveguide system with two or multiple coupling points, *Phys. Rev. A* **101**, 053855 (2020).

[10] J. Zhou, X.-L. Yin, and J.-Q. Liao, Chiral and nonreciprocal single-photon scattering in a chiral-giant-molecule waveguide-qed system, *Phys. Rev. A* **107**, 063703 (2023).

[11] A. F. Kockum, G. Johansson, and F. Nori, Decoherence-free interaction between giant atoms in waveguide quantum electrodynamics, *Phys. Rev. Lett.* **120**, 140404 (2018).

[12] L. Du, L. Guo, and Y. Li, Complex decoherence-free interactions between giant atoms, *Phys. Rev. A* **107**, 023705 (2023).

[13] X.-L. Yin, W.-B. Luo, and J.-Q. Liao, Non-markovian disentanglement dynamics in double-giant-atom waveguide-qed systems, *Phys. Rev. A* **106**, 063703 (2022).

[14] X.-L. Yin and J.-Q. Liao, Generation of two-giant-atom entanglement in waveguide-qed systems, *Phys. Rev. A* **108**, 023728 (2023).

[15] H. Yu, Z. Wang, and J.-H. Wu, Entanglement preparation and nonreciprocal excitation evolution in giant atoms by controllable dissipation and coupling, *Phys. Rev. A* **104**, 013720 (2021).

[16] A. C. Santos and R. Bachelard, Generation of maximally entangled long-lived states with giant atoms in a waveguide, *Phys. Rev. Lett.* **130**, 053601 (2023).

[17] G. Chen and A. Frisk Kockum, Simulating open quantum systems with giant atoms, *Quantum Science and Technology* **10**, 025028 (2025).

[18] L. Du, X. Wang, A. F. Kockum, and J. Splettstoesser, Dressed interference in giant superatoms: Entanglement generation and transfer, *Phys. Rev. Lett.* **135**, 223601 (2025).

[19] A. L. Grimsmo, Time-delayed quantum feedback control, *Phys. Rev. Lett.* **115**, 060402 (2015).

[20] H. Pichler and P. Zoller, Photonic circuits with time delays and quantum feedback, *Phys. Rev. Lett.* **116**, 093601 (2016).

[21] F. Caruso, V. Giovannetti, C. Lupo, and S. Mancini, Quantum channels and memory effects, *Rev. Mod. Phys.* **86**, 1203 (2014).

[22] H.-P. Breuer, E.-M. Laine, J. Piilo, and B. Vacchini, Colloquium: Non-markovian dynamics in open quantum systems, *Rev. Mod. Phys.* **88**, 021002 (2016).

[23] I. de Vega and D. Alonso, Dynamics of non-markovian open quantum systems, *Rev. Mod. Phys.* **89**, 015001 (2017).

[24] M. Yu, T.-A. Ohst, H.-C. Nguyen, and S. Nimmrichter, *Quantum memory in spontaneous emission processes* (2025), arXiv:2504.08605 [quant-ph].

[25] Y. Wang, M. Um, J. Zhang, S. An, M. Lyu, J.-N. Zhang, L.-M. Duan, D. Yum, and K. Kim, Single-qubit quantum memory exceeding ten-minute coherence time, *Nature Photonics* **11**, 646 (2017).

[26] F. Binder, L. Correa, C. Gogolin, J. Anders, and G. Adesso, *Thermodynamics in the Quantum Regime: Fundamental Aspects and New Directions*, Fundamental Theories of Physics (Springer International Publishing, 2019).

[27] D. Newman, F. Mintert, and A. Nazir, Performance of a quantum heat engine at strong reservoir coupling, *Phys. Rev. E* **95**, 032139 (2017).

[28] A. Valentini, Non-local correlations in quantum electrodynamics, *Physics Letters A* **153**, 321 (1991).

[29] J. León and C. Sabín, Generation of atom-atom correlations inside and outside the mutual light cone, *Phys. Rev. A* **79**, 012304 (2009).

[30] C. Sabín, J. J. García-Ripoll, E. Solano, and J. León, Dynamics of entanglement via propagating microwave photons, *Phys. Rev. B* **81**, 184501 (2010).

[31] H. Pichler, S. Choi, P. Zoller, and M. D. Lukin, Universal photonic quantum computation via time-delayed feedback, *Proceedings of the National Academy of Sciences* **114**, 11362 (2017).

[32] L. R. Sletten, B. A. Moores, J. J. Viennot, and K. W. Lehnert, Resolving phonon fock states in a multimode cavity with a double-slit qubit, *Phys. Rev. X* **9**, 021056 (2019).

[33] L. Guo, A. Grimsmo, A. F. Kockum, M. Pletyukhov, and G. Johansson, Giant acoustic atom: A single quantum system with a deterministic time delay, *Phys. Rev. A* **95**, 053821 (2017).

[34] G. Magnifico, M. Maffei, D. Pomarico, D. Das, P. Facchi, S. Pascazio, and F. V. Pepe, Non-markovian dynamics of generation of bound states in the continuum via single-photon scattering, *Phys. Rev. Res.* **7**, 033249 (2025).

[35] A. W. Chin, A. Rivas, S. F. Huelga, and M. B. Plenio, Exact mapping between system-reservoir quantum models and semi-infinite discrete chains using orthogonal polynomials, *Journal of Mathematical Physics* **51**, 092109 (2010).

[36] A. Strathearn, P. Kirton, D. Kilda, J. Keeling, and B. W. Lovett, Efficient non-markovian quantum dynamics using time-evolving matrix product operators, *Nature communications* **9**, 3322 (2018).

[37] V. Link, H.-H. Tu, and W. T. Strunz, Open quantum system dynamics from infinite tensor network contraction, *Phys. Rev. Lett.* **132**, 200403 (2024).

[38] D. Suess, A. Eisfeld, and W. T. Strunz, Hierarchy of stochastic pure states for open quantum system dynamics, *Phys. Rev. Lett.* **113**, 150403 (2014).

[39] Y. Tanimura and R. Kubo, Two-time correlation functions of a system coupled to a heat bath with a gaussian-markoffian interaction, *Journal of the Physical Society of Japan* **58**, 1199 (1989).

[40] Y. Tanimura, Numerically “exact” approach to open quantum dynamics: The hierarchical equations of motion (heom), *The Journal of Chemical Physics* **153**, 020901 (2020).

[41] N. Lambert, T. Raheja, S. Cross, P. Menczel, S. Ahmed, A. Pitchford, D. Burgarth, and F. Nori, Qutip-bofin: A bosonic and fermionic numerical hierarchical-equations-of-motion library with applications in light-harvesting, quantum control, and single-molecule electronics, *Phys. Rev. Res.* **5**, 013181 (2023).

[42] Y. Tanimura, Nonperturbative expansion method for a quantum system coupled to a harmonic-oscillator bath, *Phys. Rev. A* **41**, 6676 (1990).

[43] A. Ishizaki and Y. Tanimura, Quantum dynamics of system strongly coupled to low-temperature colored noise bath: Reduced hierarchy equations approach, *Journal of the Physical Society of Japan* **74**, 3131 (2005).

[44] J.-J. Ding, R.-X. Xu, and Y. Yan, Optimizing hierarchical equations of motion for quantum dissipation and quantifying quantum bath effects on quantum transfer mechanisms, *The Journal of Chemical Physics* **136**, 224103 (2012).

[45] J. Hu, R.-X. Xu, and Y. Yan, Communication: Padé spectrum decomposition of fermi function and bose function, *The Journal of Chemical Physics* **133**, 101106 (2010).

[46] J. Hu, M. Luo, F. Jiang, R.-X. Xu, and Y. Yan, Padé spectrum decompositions of quantum distribution functions and optimal hierarchical equations of motion construction for quantum open systems, *The Journal of Chemical Physics* **134**, 244106 (2011).

[47] R. Roy and T. Kailath, Esprit-estimation of signal parameters via rotational invariance techniques, *IEEE Transactions on Acoustics, Speech, and Signal Processing* **37**, 984 (1989).

[48] H. Takahashi, S. Rudge, C. Kaspar, M. Thoss, and R. Borrelli, High accuracy exponential decomposition of bath correlation functions for arbitrary and structured spectral densities: Emerging methodologies and new ap-

proaches, *The Journal of Chemical Physics* **160**, 204105 (2024).

[49] L. Cui, H.-D. Zhang, X. Zheng, R.-X. Xu, and Y. Yan, Highly efficient and accurate sum-over-poles expansion of fermi and bose functions at near zero temperatures: Fano spectrum decomposition scheme, *The Journal of Chemical Physics* **151**, 024110 (2019).

[50] H.-D. Zhang, L. Cui, H. Gong, R.-X. Xu, X. Zheng, and Y. Yan, Hierarchical equations of motion method based on fano spectrum decomposition for low temperature environments, *The Journal of Chemical Physics* **152**, 064107 (2020).

[51] M. Xu, Y. Yan, Q. Shi, J. Ankerhold, and J. T. Stockburger, Taming quantum noise for efficient low temperature simulations of open quantum systems, *Phys. Rev. Lett.* **129**, 230601 (2022).

[52] S. Vanhuffel, H. Chen, C. Decanniere, and P. Vanhecke, Algorithm for time-domain nmr data fitting based on total least squares, *Journal of Magnetic Resonance, Series A* **110**, 228 (1994).

[53] T. Aushev, A. N. Kozhinov, and Y. O. Tsybin, Least-squares fitting of time-domain signals for fourier transform mass spectrometry, *Journal of the American Society for Mass Spectrometry* **25**, 1263 (2014), pMID: 24789745.

[54] R. Hartmann, M. Werther, F. Grossmann, and W. T. Strunz, Exact open quantum system dynamics: Optimal frequency vs time representation of bath correlations, *The Journal of Chemical Physics* **150**, 234105 (2019).

[55] Z.-H. Chen, Y. Wang, X. Zheng, R.-X. Xu, and Y. Yan, Universal time-domain prony fitting decomposition for optimized hierarchical quantum master equations, *The Journal of Chemical Physics* **156**, 221102 (2022).

[56] D. Schaubert, Application of prony's method to time-domain reflectometer data and equivalent circuit synthesis, *IEEE Transactions on Antennas and Propagation* **27**, 180 (1979).

[57] M. Abramowitz and I. Stegun, *Handbook of Mathematical Functions: With Formulas, Graphs, and Mathematical Tables*, Applied mathematics series (Dover Publications, 1965).

[58] N. Van Kampen, *Stochastic Processes in Physics and Chemistry*, North-Holland Personal Library (North Holland, 2011).

[59] M. J. W. Hall, J. D. Cresser, L. Li, and E. Andersson, Canonical form of master equations and characterization of non-markovianity, *Phys. Rev. A* **89**, 042120 (2014).

[60] R. Hartmann and W. T. Strunz, Accuracy assessment of perturbative master equations: Embracing nonpositivity, *Phys. Rev. A* **101**, 012103 (2020).

[61] S. Scali, J. Anders, and L. A. Correa, Local master equations bypass the secular approximation, *Quantum* **5**, 451 (2021).

[62] A. Frisk Kockum, Quantum optics with giant atoms—the first five years, in *International Symposium on Mathematics, Quantum Theory, and Cryptography*, edited by T. Takagi, M. Wakayama, K. Tanaka, N. Kunihiro, K. Kimoto, and Y. Ikematsu (Springer Singapore, Singapore, 2021) pp. 125–146.

[63] M. Campisi, P. Talkner, and P. Hänggi, Fluctuation theorem for arbitrary open quantum systems, *Phys. Rev. Lett.* **102**, 210401 (2009).

[64] A. Rivas, Strong coupling thermodynamics of open quantum systems, *Phys. Rev. Lett.* **124**, 160601 (2020).

[65] L. Guo, A. F. Kockum, F. Marquardt, and G. Johansson, Oscillating bound states for a giant atom, *Phys. Rev. Res.* **2**, 043014 (2020).

[66] L. Li and X. Cao, Coherent destruction of tunneling of quantum energy transport in a driven nonequilibrium spin-boson model, *Phys. Rev. B* **110**, 075403 (2024).

[67] M. Ritter, D. M. Long, Q. Yue, A. Chandran, and A. J. Kollár, Autonomous stabilization of floquet states using static dissipation, *Phys. Rev. X* **15**, 031028 (2025).

[68] C. Bäcker, K. Beyer, and W. T. Strunz, Local disclosure of quantum memory in non-markovian dynamics, *Phys. Rev. Lett.* **132**, 060402 (2024).

[69] H. Breuer and F. Petruccione, *The Theory of Open Quantum Systems* (Oxford University Press, 2002).

[70] M. Lobejko, M. Winczewski, G. Suárez, R. Alicki, and M. Horodecki, Corrections to the hamiltonian induced by finite-strength coupling to the environment, *Phys. Rev. E* **110**, 014144 (2024).

## Appendix A: Exact master equation in RWA at zero temperature

Here we derive the master equation (7) based on the exact solution for the evolution of the giant atom and the SAW field under the RWA at zero temperature. The RWA allows us to drop the counter-rotating interaction terms in the atom-bath Hamiltonian (2), so that in the interaction picture with respect to  $\hat{H}_0 = \hbar\omega_0|e\rangle\langle e| + \hbar\sum_{j=R,L}\int_0^\infty d\omega\omega\hat{a}_{j\omega}^\dagger\hat{a}_{j\omega}$ , the interaction Hamiltonian reduces to

$$\hat{H}_I(t) = \hbar\sum_{j=R,L}\int_0^\infty d\omega\sqrt{\frac{\gamma(\omega)}{\pi}}\cos\left(\frac{\omega\tau}{2}\right)\left[\hat{a}_{j\omega}^\dagger e^{-i(\omega_0-\omega)t}\hat{\sigma}_- + \hat{a}_{j\omega}e^{i(\omega_0-\omega)t}\hat{\sigma}_+\right]. \quad (\text{A1})$$

Given that the phonon field is initially in the vacuum state and the total excitation number of atom and field is conserved, there can be at most a single phonon excitation present at any time  $t$ . A global pure state can thus be described by the ansatz

$$|\Psi(t)\rangle = \sum_{j=R,L}\int d\omega\alpha_{j\omega}(t)\hat{a}_{j\omega}^\dagger|g,0\rangle + e(t)|e,0\rangle + g(0)|g,0\rangle, \quad (\text{A2})$$

with the initial condition  $\alpha_\omega(0) = 0$ . The amplitude of the  $|g,0\rangle$  component remains constant in time, as  $\hat{H}_I(t)|g,0\rangle = 0$ . Using the Schrödinger equation  $i\hbar\partial_t|\Psi(t)\rangle = \hat{H}_I(t)|\Psi(t)\rangle$ , we obtain the coupled equations of motion for the

probability amplitudes

$$\dot{e}(t) = -i \sum_{j=1,2} \int_0^\infty d\omega \sqrt{\frac{\gamma(\omega)}{\pi}} \cos\left(\frac{\omega\tau}{2}\right) \alpha_{j\omega}(t) e^{i(\omega_0-\omega)t}, \quad (\text{A3})$$

$$\dot{\alpha}_{j\omega}(t) = -i \sqrt{\frac{\gamma(\omega)}{\pi}} \cos\left(\frac{\omega\tau}{2}\right) e(t) e^{-i(\omega_0-\omega)t}. \quad (\text{A4})$$

By formally solving  $\alpha_{j\omega}(t)$  and substituting the result into Eq. (A3), we obtain an integro-differential equation for the amplitude  $e(t)$ . Writing  $e(t) = G(t)e(0)$  in terms of a propagator function  $G(t)$ , the equation can be stated as

$$\dot{G}(t) = - \int_0^t ds C(s) G(t-s) e^{i\omega_0 s}, \quad (\text{A5})$$

with initial condition  $G(0) = 1$ . Here,  $C(s)$  is the BCF of the phonon field at zero temperature,

$$C(s) = \frac{1}{\pi} \int_0^\infty d\omega 2\gamma(\omega) \cos^2\left(\frac{\omega\tau}{2}\right) e^{-i\omega s}. \quad (\text{A6})$$

The solution of  $G(t)$  can be found through a Laplace transform or a Fourier transform with appropriate boundary conditions [33]. From this, the reduced density matrix of the giant atom in the interaction picture can be obtained by tracing over the field,

$$\tilde{\rho}_S(t) = \text{tr}_f\{|\Psi(t)\rangle\langle\Psi(t)|\} = \begin{bmatrix} \rho_{ee}(t) & \rho_{eg}(t) \\ \rho_{ge}(t) & \rho_{gg}(t) \end{bmatrix} = \begin{bmatrix} |G(t)|^2 \rho_{ee}(0) & G(t) \rho_{eg}(0) \\ G^*(t) \rho_{eg}^*(0) & 1 - |G(t)|^2 \rho_{ee}(0) \end{bmatrix}. \quad (\text{A7})$$

This describes how the populations and the coherence of the giant atom evolve in time, governed by the function  $G(t)$ . It is important to note that, although these equations have been derived assuming a pure initial product state, they are also valid for any mixed initial state of the giant atom. This generality arises from the fact that a mixed state can be represented as a convex linear combination of pure states, and the function  $G(t)$  is independent of the initial condition.

To arrive at a generator of the exact time evolution, we can simply take the time derivative of (A7) and express it in terms of a linear superoperator,  $d\tilde{\rho}_S(t)/dt = \mathcal{K}(t)\tilde{\rho}_S(t)$ . After a few steps of algebra, we find the closed form,

$$\mathcal{K}(t)\tilde{\rho}_S(t) = -ih(t)[\hat{\sigma}_+\hat{\sigma}_-, \tilde{\rho}_S(t)] + \gamma_-(t)\mathcal{D}[\hat{\sigma}_-]\tilde{\rho}_S(t). \quad (\text{A8})$$

Here,  $h(t) = -\text{Im}[\dot{G}(t)/G(t)]$  is the Lamb shift of the system energy and  $\mathcal{D}[\hat{\sigma}_-]\tilde{\rho}_S(t) = 2\hat{\sigma}_-\tilde{\rho}_S(t)\hat{\sigma}_+ - \{\hat{\sigma}_+\hat{\sigma}_-, \tilde{\rho}_S(t)\}$  is the dissipator describing spontaneous emission with a time-dependent decay rate  $\gamma_-(t) = -\text{Re}[\dot{G}(t)/G(t)]$ . Transforming back to the Schrödinger picture, we obtain the master equation (7) in the main text.

## Appendix B: Redfield master equation in RWA at zero temperature

Here we derive the explicit form of the Redfield master equation for the giant atom under RWA at zero temperature, which is compared to the exact solution in the main text. The Redfield master equation is a time-local differential equation for the reduced state of an open quantum system that describes its evolution to lowest perturbative order in the weak coupling to a large reservoir [69]. In the interaction picture, it is given by

$$\frac{d}{dt}\tilde{\rho}_S(t) = -\frac{1}{\hbar^2} \int_0^t ds \text{tr}_B \left\{ [\hat{H}_I(t), [\hat{H}_I(s), \tilde{\rho}_S(t) \otimes \rho_B(0)]] \right\}. \quad (\text{B1})$$

Inserting the interaction-picture Hamiltonian for our case,  $\hat{H}_I(t) = \hbar\tilde{\sigma}_x(t)\hat{B}(t)$  with  $\tilde{\sigma}_x(t) = \hat{\sigma}_-e^{-i\omega_0 t} + h.c.$  and  $\hat{B}(t)$  given in (2), the master equation can be expressed as

$$\frac{d}{dt}\tilde{\rho}_S(t) = - \int_0^t dt' \left\{ C(t-t') [\hat{\sigma}_x(t), \hat{\sigma}_x(t')\tilde{\rho}_S(t)] + \text{h.c.} \right\}. \quad (\text{B2})$$

Here, the properties of the phonon bath are encoded in the BCF  $C(t)$ . Assuming a thermal initial state  $\rho_B(0)$  at inverse temperature  $\beta = \hbar/k_B T$ , the BCF reads as

$$C(s) = \langle \tilde{B}(t)\tilde{B}(t+s) \rangle = \sum_{j=R,L} \int_0^\infty d\omega \frac{\gamma(\omega)}{\pi} \cos^2\left(\frac{\omega\tau}{2}\right) \left[ \frac{2\cos\omega s}{e^{\beta\omega} - 1} + e^{-i\omega s} \right] = \frac{1}{\pi} \int_{-\infty}^\infty d\omega J(\beta, \omega) e^{-i\omega s},$$

introducing the effective bath spectral density

$$J(\beta, \omega) := \frac{2\gamma(\omega)}{1 - e^{-\beta\omega}} \cos^2\left(\frac{\omega\tau}{2}\right), \text{ setting } \gamma(\omega) := -\gamma(-\omega) \text{ for } \omega < 0. \quad (\text{B3})$$

Transforming back to the Schrödinger picture, the master equation becomes

$$\frac{d}{dt}\rho_S(t) = -i\omega_0[\hat{\sigma}_+\hat{\sigma}_-, \rho_S(t)] - \int_0^t ds\{C(s)[\hat{\sigma}_x, \hat{\sigma}_x(-s)\rho_S(t)] + \text{h.c.}\}, \quad (\text{B4})$$

where the  $\hat{\sigma}_x$  and  $\hat{\sigma}_\pm$  without time argument refer to the Schrödinger-picture operators. Finally, we can expand the remaining  $\hat{\sigma}_x(-s) = \hat{\sigma}_-e^{i\omega_0 s} + \hat{\sigma}_+e^{-i\omega_0 s}$ , which leads to

$$\frac{d}{dt}\rho_S(t) = -i\omega_0[\hat{\sigma}_+\hat{\sigma}_-, \rho_S(t)] + \{\Gamma_+(t)[\hat{\sigma}_+\rho_S(t), \hat{\sigma}_x] + \text{h.c.}\} + \{\Gamma_-(t)[\hat{\sigma}_-\rho_S(t), \hat{\sigma}_x] + \text{h.c.}\}, \quad (\text{B5})$$

with the time-dependent coefficients  $\Gamma_\pm(t) = \int_0^t ds C(s) e^{\mp i\omega_0 s}$ . Under the RWA, we drop all counter-rotating terms and keep only those operator products containing both  $\hat{\sigma}_+$  and  $\hat{\sigma}_-$ , resulting in

$$\frac{d}{dt}\rho_S(t) \approx -i[\omega_0\hat{\sigma}_+\hat{\sigma}_- + \text{Im}[\Gamma_+(t)]\hat{\sigma}_-\hat{\sigma}_+ + \text{Im}[\Gamma_-(t)]\hat{\sigma}_+\hat{\sigma}_-, \rho_S(t)] + \text{Re}[\Gamma_+(t)]\mathcal{D}[\hat{\sigma}_+]\rho_S(t) + \text{Re}[\Gamma_-(t)]\mathcal{D}[\hat{\sigma}_-]\rho_S(t). \quad (\text{B6})$$

In this form, it is evident that the real and imaginary parts of  $\Gamma_\pm(t)$  determine the dissipative and coherent contributions, respectively. At zero temperature, the coefficient  $\Gamma_+(t)$  becomes strongly suppressed compared to  $\Gamma_-(t)$  and can thus be neglected. We are left with

$$\frac{d}{dt}\rho_S(t) = -i(\omega_0 + \text{Im}[\Gamma_-(t)])[\hat{\sigma}_+\hat{\sigma}_-, \rho_S(t)] + \text{Re}[\Gamma_-(t)]\mathcal{D}[\hat{\sigma}_-]\rho_S(t), \quad (\text{B7})$$

which we use for comparison with our exact results in Sec. V of the main text.

### Appendix C: Calculation of mean-force Hamiltonian

Here we present a perturbative method for evaluating the Hamiltonian of mean force. From this, the corresponding Gibbs state can be constructed and compared with the stationary state obtained numerically via HEOM in Sec. VI. The Hamiltonian of mean force is defined as [63, 64]

$$\hat{H}_S^* = -\frac{1}{\tilde{\beta}} \log \left[ \frac{\text{tr}_B\{e^{-\tilde{\beta}\hat{H}}\}}{\mathcal{Z}_B} \right], \quad (\text{C1})$$

where  $\mathcal{Z}_B$  is partition function of the bath and here  $\tilde{\beta} = \beta/\hbar = 1/k_B T$ . To proceed, we apply the imaginary-time Dyson identity [70]

$$e^{-\tilde{\beta}\hat{H}} = e^{-\tilde{\beta}(\hat{H}_S + \hat{H}_B)} \mathcal{T} e^{-\int_0^{\tilde{\beta}} d\tilde{t} \hat{H}_I(\tilde{t})}, \quad (\text{C2})$$

with the shorthand notation  $\hat{H}_I(\tilde{t}) = e^{\tilde{t}(\hat{H}_S + \hat{H}_B)} \hat{H}_I e^{\tilde{t}(\hat{H}_S + \hat{H}_B)}$  and  $\mathcal{T}$  is the time-ordering operator. Notice that the imaginary time variable  $\tilde{t}$  is now given in units of inverse energy. Using the identity, the Hamiltonian of mean force can be written in the Dyson-expanded form

$$\hat{H}_S^* = -\frac{1}{\tilde{\beta}} \log \left[ e^{-\tilde{\beta}H_s} \langle \mathcal{T} e^{-\int_0^{\tilde{\beta}} d\tilde{t}' \hat{H}_I(\tilde{t}')} \rangle_B \right] = \hat{H}_S - \frac{1}{\tilde{\beta}} \log \langle \mathcal{T} e^{-\int_0^{\tilde{\beta}} d\tilde{t}' \hat{H}_I(\tilde{t}')} \rangle_B, \quad (\text{C3})$$

where  $\langle \cdot \rangle_B$  denotes the thermal expectation value over the bath and

$$\langle \mathcal{T} e^{-\int_0^{\tilde{\beta}} d\tilde{t}' \hat{H}_I(\tilde{t}')} \rangle_B = 1 - \int_0^{\tilde{\beta}} d\tilde{t} \langle \hat{H}_I(\tilde{t}) \rangle_B + \int_0^{\tilde{\beta}} d\tilde{t}_1 \int_0^{\tilde{t}_1} d\tilde{t}_2 \langle \hat{H}_I(\tilde{t}_1) \hat{H}_I(\tilde{t}_2) \rangle_B + \dots \quad (\text{C4})$$

The first-order contribution  $\langle \hat{H}_I(\tilde{t}) \rangle_B$  typically vanishes, and does so in our case. For moderate coupling strengths, a second-order truncation provides an accurate approximation. We will show that this approximation is sufficient for

the coupling regime considered in Fig. 5(b). Consider the interaction between the giant atom and SAWs in Eq. (2), the second-order term is given by

$$\begin{aligned} \int_0^{\tilde{\beta}} d\tilde{t}_1 \int_0^{\tilde{t}_1} d\tilde{t}_2 \langle \hat{H}_I(\tilde{t}_1) \hat{H}_I(\tilde{t}_2) \rangle_B &= I_1(\tilde{\beta}) \hat{\sigma}_+ \hat{\sigma}_- + I_2(\tilde{\beta}), \quad \text{with} \\ I_1(\tilde{\beta}) &= \hbar^2 \int_0^{\tilde{\beta}} d\tilde{t}_1 \int_0^{\tilde{t}_1} d\tilde{s} \tilde{C}(\tilde{s}) \sinh \hbar\omega_0 \tilde{s}, \\ I_2(\tilde{\beta}) &= \hbar^2 \int_0^{\tilde{\beta}} d\tilde{t}_1 \int_0^{\tilde{t}_1} d\tilde{s} \tilde{C}(\tilde{s}) [\cosh \hbar\omega_0(2\tilde{t}_1 - \tilde{s}) + e^{-\hbar\omega_0 \tilde{s}}]. \end{aligned} \quad (\text{C5})$$

Here,  $\tilde{C}(s)$  is the BCF in the imaginary-time interaction picture, which for our Ohmic setting is given by

$$\begin{aligned} \tilde{C}(\tilde{s}) &= \frac{\eta}{2\pi\hbar^2\tilde{\beta}^2} \left\{ 2\Psi\left[1, \frac{1+\tilde{s}\hbar\omega_c}{\tilde{\beta}\hbar\omega_c}\right] + 2\Psi\left[1, 1-\frac{\tilde{s}}{\tilde{\beta}} + \frac{1}{\tilde{\beta}\hbar\omega_c}\right] + \Psi\left[1, \frac{1+\tilde{s}\hbar\omega_c-i\tau\omega_c}{\tilde{\beta}\hbar\omega_c}\right] + \Psi\left[1, \frac{1+\tilde{s}\hbar\omega_c+i\tau\omega_c}{\tilde{\beta}\hbar\omega_c}\right] \right. \\ &\quad \left. + \Psi\left[1, \frac{1+(\tilde{\beta}-\tilde{s})\hbar\omega_c-i\tau\omega_c}{\tilde{\beta}\hbar\omega_c}\right] + \Psi\left[1, \frac{1+(\tilde{\beta}-\tilde{s})\hbar\omega_c+i\tau\omega_c}{\tilde{\beta}\hbar\omega_c}\right] \right\}. \end{aligned} \quad (\text{C6})$$

We evaluate  $I_1(\tilde{\beta})$  and  $I_2(\tilde{\beta})$  numerically. Thus, the mean-force Hamiltonian to second order is given by

$$\begin{aligned} \hat{H}_S^* &\approx \hat{H}_S + \frac{\delta\omega(\tilde{\beta})}{2} \hat{\sigma}_z + c(\tilde{\beta}), \quad \text{with} \\ \delta\omega(\tilde{\beta}) &= -\frac{\log[1+I_1(\tilde{\beta})+I_2(\tilde{\beta})]-\log[1+I_2(\tilde{\beta})]}{\tilde{\beta}}, \\ c(\tilde{\beta}) &= -\frac{\log[1+I_1(\tilde{\beta})+I_2(\tilde{\beta})]+\log[1+I_2(\tilde{\beta})]}{2\tilde{\beta}}. \end{aligned} \quad (\text{C7})$$

Note that the offset term  $c(\tilde{\beta})$  does not affect the thermodynamical properties and therefore can be neglected. The corresponding Gibbs state is  $\rho_S^* = e^{-\tilde{\beta}\hat{H}_S^*}/\mathcal{Z}_S^*$  with  $\mathcal{Z}_S = \text{tr}_S(e^{-\tilde{\beta}\hat{H}_S^*})$ . The excited-state probability is then obtained as

$$P_{ee}^* = \langle e | \rho_S^* | e \rangle \approx \left( 1 + e^{\beta\omega_0 - \log[1+I_1(\tilde{\beta})+I_2(\tilde{\beta})]+\log[1+I_2(\tilde{\beta})]} \right)^{-1}. \quad (\text{C8})$$

Table I compares the excited-state populations of the giant atom predicted by the second-order mean-force Hamiltonian with those obtained from HEOM in the stationary regime, as well as with the Gibbs-state population of the bare system Hamiltonian at various temperatures. At finite temperatures and particularly in the higher-temperature regime, the second-order mean-force Hamiltonian yields excited-state populations that almost exactly coincide with the HEOM results, and both closely follow the corresponding Gibbs-state values for the considered coupling strength. At lower temperatures, small deviations emerge, reflecting the increasing importance of temperature-dependent and higher-order corrections that are not fully captured at second order.

|                 | $\beta\omega_0 = \infty$ | $\beta\omega_0 = 1.0$ | $\beta\omega_0 = 0.5$ | $\beta\omega_0 = 0.1$ |
|-----------------|--------------------------|-----------------------|-----------------------|-----------------------|
| $P_{ee}$        | 0.009                    | 0.272                 | 0.378                 | 0.475                 |
| $P_{ee}^*$      | 0                        | 0.271                 | 0.378                 | 0.475                 |
| $P_{ee}^{(th)}$ | 0                        | 0.269                 | 0.377                 | 0.475                 |

TABLE I. Comparison of the stationary excited-state populations obtained from HEOM, the Hamiltonian of mean force, and the bare system Hamiltonian at several temperatures. Please refer to Fig. 5(b) of main text for the parameter settings.